DOI: 10.1002/ ((please add manuscript number))
Article type: Full Paper

Enhancing Long-Term Thermal Stability of Non-Fullerene Organic Solar Cells Using Self-Assembly Amphiphilic Dendritic Block Copolymer Interlayers

Li-Yun Su,[a,b,c] *Hsin-Hsiang Huang,*[b,d,e] *Yan-Cheng Lin,*[a] *Guan-Lin Chen,*[b] *Wen-Chang Chen,*[a,f] *Wei Chen,*[e,g] *Leeyih Wang,*[b,h,*] *and Chu-Chen Chueh*[a,f,*]

[a] Dr. L. Y. Su, Y. C. Lin, Prof. W. C. Chen, Prof. C. C. Chueh
Department of Chemical Engineering, National Taiwan University, Taipei 10617, Taiwan

[b] Dr. L. Y. Su, H. H. Huang, G. L. Chen, Prof. L. Wang
Center for Condensed Matter Sciences, National Taiwan University, Taipei 10617, Taiwan

[c] Dr. L. Y. Su
Center for Integrated Nanotechnologies, Los Alamos National Laboratory, Los Alamos, New Mexico 87545, USA

[d] H. H. Huang
Department of Material Science and Engineering, National Taiwan University, Taipei 10617, Taiwan

[e] H. H. Huang, Dr. W. Chen
Materials Science Division, Argonne National Laboratory, Lemont, Illinois 60439, USA

[f] Prof. W. C. Chen, Prof. C. C. Chueh
Advanced Research Center for Green Materials Science and Technology, National Taiwan University, Taipei 10617, Taiwan

[g] Dr. W. Chen
Pritzker School of Molecular Engineering, University of Chicago, Chicago, Illinois 60637, USA.

[h] Prof. L. Wang
Center of Atomic Initiative for New Materials, National Taiwan University, Taipei 10617, Taiwan

[*]Corresponding author. Email: leewang@ntu.edu.tw; cchueh@ntu.edu.tw

Keywords: Dendritic block copolymers, self-assembly, metal nanoparticles, interfacial modification, thermal stability

As the power conversion efficiency (PCE) of organic photovoltaics (OPVs) has surpassed 17%, this technology faces the challenges in improving device's long-term durability. Herein, interfacial engineering is demonstrated to largely improve the thermal stability of non-fullerene bulk-heterojunction (NFA BHJ) OPVs to a practical level. An amphiphilic dendritic block copolymer (DBC) is developed through a facile coupling method and employed as the surface modifier of ZnO electron-transporting layer in inverted OPVs. Besides showing distinct self-assembly behavior, the synthesized DBC possesses high compatibility with plasmonic Au nanoparticles (NPs) due to the constituent malonamide and ethylene oxide units. The hybrid DBC@AuNPs interlayer is shown to improve device's PCE from 14.0% to 15.4% because it enables better energy level alignment and improves interfacial compatibility at the ZnO/BHJ interface. Moreover, the DBC@AuNPs interlayer is revealed to not only improve the interfacial thermal stability at the ZnO/BHJ interface but also endow a more ideal BHJ morphology with an enhanced thermal robustness. The derived device reserves 77% of initial PCE after thermal aging at 65°C for 3,000 hours and yields an extended T_{80} lifetime of > 1,100 hours when stored at a constant thermal condition at 65°C, outperforming the control device. Finally, the device is evaluated to possess a T_{80} lifetime of over 1.79 years at room temperature (298 K) when stored in an inert condition, showing great potential for commercialization.

1. Introduction

Over the past decade, organic photovoltaics (OPVs) have achieved significant progress in power conversion efficiency (PCE) and the state-of-the-art PCE of bulk-heterojunction (BHJ) OPVs has approached 17%.[1] Such rapid advance is promoted by the innovations of photoactive materials, interfacial materials, and device engineering.[2] Among them, the recent successful exploitation of non-fullerene acceptor (NFA) plays the most critical role while the exploration of novel interfacial layers is continuously proceeded to further enhance the overall performance and stability.[2a] Interface engineering has been proven to not only improve the charge-collection efficiency and carrier selectivity in the device but also endow better energy-level alignment at the organic/metal interface.[3] Meanwhile, it might also optimize the interpenetrating morphology of the photoactive BHJ layer by improving the compatibility at the BHJ-associated interface.[3]

Benefitting from the high flexibility in structural design and more compatible surface energy to organic semiconductors, organic interfacial materials have been vigorously developed in the past few years. To date, numerous organic interfacial materials have been developed based on two main systems. One is conjugated system, for which the most famous materials are poly[(9,9-bis(3'-(N,N-dimethylamino)propyl)-2,7-fluorene)-alt-2,7-(9,9-dioctylfluorene)] (PFN)-based derivatives.[4] However, their production cost is quite high. The other is non-conjugated system, for which the most renowned materials are polyethylenimine (PEI)-based derivatives and their ethoxylated analogues (PEIEs).[5] Despite the insulating nature, their polyelectrolyte-like property has been proven to effective tune the interfacial dipole at the organic/metal interface.

Beyond these two systems, we note that there is an alternative class of interfacial materials based on polyelectrolyte block copolymers (BCPs) that can comprise conjugated segments, non-conjugated segments or a combination of them, and have demonstrated promising results in some cases.[6] From the chemical aspect, the polymerization of BCP possesses a precise and well-controllable feature. From the physical aspect, the distinctly different polarity of the constituent blocks endows BCP with diverse self-assembly behaviors, which can be beneficial for improving the interfacial compatibility/morphology in the device.[6] Notably, as being similar to BCP, dendritic block copolymers (DBCs) with a high and controlled number of peripheral groups are more easier to synthesize and can offer a high degree of molecular uniformity, specific size, and shape characteristics. In addition, their functionality can be similarly manipulated by tailoring the constituent segments. All these merits render the DBCs as potential interfacial materials for OPVs. However, related exploration has been rarely investigated in the literature and only limited to the hyper-branched analogues.[7]

Besides improving PCE, recent researches regarding interface engineering have been focused on understanding its impact on device’s long-term stability, another pivotal factor for the commercialization of OPVs.[8] Many environmental issues have been reported to cause device degradation, such as heat, light, humidity, and oxygen, and these issues need to be properly solved to realize the actual outdoor applications of OPVs. As mentioned earlier, interface engineering could indirectly optimize the interpenetrating morphology of a BHJ layer.[3] Therefore, it might make great contribution in enhancing device's overall stability as well. The BHJ morphology has been known to strongly correlate with device's efficiency;[9] however, it is generally in a thermally metastable state. It thus would be easily affected by external impulses to cause unfavorable phase separation, resulting in degraded efficiency and inferior stability.[10] Thus far, various approaches have been proposed to address these issues, especially for the thermal instability of BHJ blends, such as selecting suitable donor/acceptor pairs,[11] reducing crystallinity of polymer donors or acceptors,[12] introducing a "molecular lock",[8d, 13] crosslinking the photoactive components,[14] etc. Nevertheless, relevant approaches based on proper interfacial engineering has not been widely examined in the literature. Regarding the unique self-assembly features of DBCs and the flexibility in the structure design, we thus envisage that the DBC-based interlayer can serve as a thermally stable interlayer and, meanwhile, modulate the BHJ morphology to enhance device's long-term thermal stability.

Based on this goal, in this study, we develop an amphiphilic DBC comprising a hydrophobic moiety based on azetidine-2,4-dione functionalized high generations of dendrons and a hydrophilic moiety based on Jeffamines®ED2003 through a facile coupling method, and examine its interlayer function in inverted NFA BHJ OPVs, modifying the surface of inorganic ZnO electron-transporting layer (ETL). Owing to the different polarity of the constituent blocks, the synthesized DBC shows distinct self-assembly behavior. We show that the optimized DBC-based device can yield a slight improvement in PCE from 14.0% to 14.5% in the PM6:Y6 BHJ system due to the improved interfacial property across the BHJ/ZnO interface. Moreover, due to the constituent malonamide and ethylene oxide units, the synthesized DBC possesses high compatibility with plasmonic gold nanoparticles (Au NPs). The hybrid DBC@AuNPs interlayer can further modulate the interfacial properties to promote the PCE to 15.4%. Overall, the enhancement introduced by DBC is attributed to the better energy level alignment and improved interfacial compatibility between the BHJ layer and ZnO ETL, which reduces charge recombination in the device. Last but not least, we demonstrate that the hybrid DBC@AuNPs interlayer not only improves the interfacial thermal stability at the BHJ/ZnO interface but also endows a more ideal BHJ morphology with an enhanced thermal robustness. As a result, the DBC@AuNPs-based device is show to reserve 77% of initial PCE after thermal aging at 65°C for 3,000 hours, outperforming control device. Further, it possesses an extended T_{80} lifetime of > 1,100 hours when stored at a constant thermal condition at 65°C. Finally, we unveil that the T_{80} lifetime of the device at room temperature (298 K) can be over 1.79 years when stored in an inert condition. Our results provide a simple method to enhance the long-term thermal stability of NFA BHJ OPVs.

2. Results and Discussion

2.1. Preparation and self-assembly behavior of DBC and its hybridization with Au NPs

The amphiphilic DBC studied in this work was prepared through a facile coupling of a hydrophobic moiety based on azetidine-2,4-dione functionalized dendrons (G2.5) with a hydrophilic moiety based on Jeffamines®ED2003 (abbreviated as ED2003 hereafter) (**Figure 1a-1b**). Its synthetic details were described in Supplementary Note 1 and relevant structural characterizations and properties were provided in **Figure S1-S3** and **Table S1**. **Figure S4** presented the differential scanning calorimetry (DSC) curves of the constituent blocks (G2.5 and ED2003) and the synthesized DBC, which were measured at a heating rate of 10 °C/min under nitrogen atmosphere. As seen, DBC displayed two phase transition temperatures (T_{ph}) at 36 °C and 84 °C, which arises from the transition temperature of ED2003 (T_m = 34°C) and G2.5 (T_g = 58°C), respectively. The observed positively-deviated T_phs are apparently resulted from the interpenetrating of the micro-separated ED2003 and G2.5 domains, which confines their molecular motion and thermal relaxation.

Due to the amphiphilic feature, DBC should be able to self-assemble into an extensive range of structures *via* solvent selections. We thus investigate its molecular self-assembling behavior in 2-methoxyethanol, which is a good solvent for the ED2003 block while is a poor solvent for the G2.5 block. The average molecular shapes adopted by amphiphilic molecules with the corresponding self-assemblies are herein expounded according to Israelachvili's famous shape factor or critical packing parameter, CPP (γ).[15] The γ correlates with the optimum values of molecular volume (V), cross sectional area at the hydrocarbon water interface (a_0), and chain length (l_c) in a relation of $\gamma = V/a_0l_c$. The calculated γ for DBC is lower than 1, suggesting that it adopts a cone shape (normal phase) structure as illustrated in **Figure 1c**. Based on the CPP theory, the DBC self-assemblies are portrayed in **Figure 1d**. Next, transmission electron microscope (TEM) and dynamic light scattering (DLS) analysis were conducted to confirm the configuration and size of the DBC self-assemblies. As seen in **Figure 1e**, slight contrast difference exists between the inner and outer zone of the self-assembled micelles. This result confirms the core-shell structure of the formed micelles, wherein the shell consists of the hydrophilic ED2003 block and the core consists of the hydrophobic G2.5 block (**Figure 1d**). Besides, the micelles exhibit a narrow distribution in dimension as shown in **Figure 1f**. More details regarding the discussion of self-assembly behavior of DBC are described in Supplementary Note 2.

It is worthwhile noting that numerous works have unveiled the advantageous effects of blending metal NPs into OPVs,[16] in which metal NPs can be added into the BHJ layer or charge-transporting layers (CTLs) to improve the electronic properties at associated interfaces or to enhance the light-harvesting efficiency of the device through plasmonic effects.[17] Since the constituent malonamide and ethylene oxide units can form intense bonding with Au NPs, the studied DBC should possess high compatibility with Au NPs to enable their homogeneous dispersion inside it, serving as a good platform for incorporating Au NPs into OPVs. We thus accordingly prepared a hybrid DBC@AuNPs film. To confirm the presence of Au NPs in the

DBC matrix and to elucidate the interactions between them, X-ray photoelectron spectroscopy (XPS) measurement analysis was conducted. As shown in **Figure 1g-1i**, the DBC@AuNPs film displayed two conspicuous peaks at 83.5 eV and 87.2 eV, corresponding to $Au4f_{5/2}$ and $Au4f_{7/2}$, respectively. These doublet peaks possess a difference in binding energies equal to 3.7 eV, which is characteristic to metallic Au^0.[27a] For the O1s spectrum, wherein the DBC film displayed a strong peak at 531.1 eV, corresponding to the C-O bond of ethylene oxide units in ED2003. This peak is positively shifted to 531.6 eV in the DBC@AuNPs film, affirming the intense interaction between DBC and Au NPs. Based on this result, the Au NPs are supposed to disperse in the shell of the self-assembled DBC micelles as depicted in **Figure 1d**, in which Au NPs possess continuous pathway to facilitate the associated plasmonic effect. The thermal property of DBC@AuNPs is also characterized to confirm the interaction between ED2003 and Au NPs, and the relevant thermal decomposition temperatures (T_d, 5% weight loss temperature) and T_{ph}s were summarized in **Table S1**. DBC@AuNPs showed elevated T_d and T_{ph}s over the pristine DBC, wherein the two T_{ph}s of DBC were increased to 42 and 86 °C (associated with an enthalpy of 20.6 and 7.25 J/g) after hybridizing with Au NPs (**Figure 1j**). These increased T_{ph}s clearly verify the intermolecular interactions between DCB and Au NPs.

2.2. Applications in NFA BHJ OPVs

The DBC and DBC@AuNPs films are then applied as the interface modifiers of ZnO ETL in the devices because ZnO ETL has been identified to have a defective surface and to possess unfavorable compatibility to organic BHJ systems.[3, 18] Prior to device fabrication, the surface energy of the studied ETLs was first analyzed to elucidate the compatibility between them and the active layer. Herein, distilled H_2O and glycerol are used as the probing liquids and the total surface energy (Υ_{total}) is equal to the sum of dispersive energy ($\Upsilon_{\text{dispersive}}$) and polar energy ($\Upsilon_{\text{polar}}$). **Table S2** summarized the relevant date, wherein Υ_{total} of the studied samples were measured using contact angle goniometry coupled with Wu model.[19] Note that, Υ_{total} of the parent ED2003 and G2.5 blocks are 75.82[20] and 33.89 mN/m,[21] respectively. As shown, the $\Upsilon_{\mathrm{total}}$ of the ZnO ETL was 55.23 mN/m, being incompatible to the value (31.65 mN/m) of the bare PM6:Y6 BHJ blend. However, after coating with thin DBC and DBC@AuNPs layers, the corresponding $\Upsilon_{\mathrm{total}}$ was reduced to 33.92 and 32.31 mN/m, respectively. Such reduction in $\Upsilon_{\mathrm{total}}$ clearly improves the interfacial compatibility at the ZnO/BHJ interface and is favorable for forming more ideal BHJ morphology. Besides, this result also indicates that the DBC has a higher probability to land on the ZnO surface in the form of self-assembled micelles rather than extended polymer chain. On the other hand, because the constituent hydrophilic ED2003 block has been reported to effectively tune the interfacial dipole at the metal interface,[20] we then examined the WF tuning capability of the DBC and DBC@AuNPs interlayer by using ultraviolet photoelectron spectroscopy (UPS). The relevant results were presented in **Figure S5**. As can be seen, the WF (-4.76 eV) of the pristine ZnO ETL was upshifted to -4.40 eV and -4.43 eV after coating with thin DBC and DBC@AuNPs interlayers, respectively. This upward-shifted WF can favor the electron transfer across the ZnO/BHJ interface due to better energy-level alignment (**Figure 2a**). Based on these results, we can conclude that the amphiphilic DBC possesses several advantages, such as tuning WF, improving BHJ morphology, acceptable thermal property, and affording uniform blending of Au NPs. All of them are beneficial for reducing charge recombination and enhancing the long-term stability of the derived device.

We next fabricated inverted OPVs based on the PM6:Y6 BHJ blend using DBC/DBC@AuNPs-modified ZnO ETLs (**Figure 2a**). The current density-voltage (J-V) curves of the fabricated devices measured under AM 1.5G illumination are presented in **Figure 2b**, and their relevant photovoltaic parameters (open-circuit voltage (V_{oc}), short- circuit current (J_{sc}), and fill factor (FF)) are summarized in **Table 1**. As seen, the DBC@AuNPs device delivered the highest PCE of 15.40 % (V_{oc} = 0.818 V, J_{sc} = 25.70 mA cm^{-2}, and FF = 0.73) and the DBC device gave a lower PCE of 14.50 % (V_{oc} = 0.809 V, J_{sc} = 24.90 mA cm^{-2}, and FF = 0.72), while the control ZnO device yielded the lowest PCE of 13.96 % (V_{oc} = 0.807 V, J_{sc} =

24.50 mA cm^{-2}, $FF = 0.71$). All photovoltaic parameters are apparently improved after using DBC and DBC@AuNPs interlayers, revealing their efficacy in facilitating the interfacial electronic properties across the ZnO/BHJ interface. **Figure S6** shows the dark currents of these fabricated devices, wherein the ZnO device displayed the largest dark current than the other two devices. It suggests that both DBC and DBC@AuNPs interlayers effectively suppress the interfacial charge recombination by passivating the defective states on ZnO surface.

To probe the charge recombination behavior in our fabricated devices, their respective photocurrent density (J_{ph}) as a function of effective voltage (V_{eff}) was plotted and presented in **Figure 2c**. Note that J_{ph} is calculated from $J_{ph} = J_L - J_D$, where J_L and J_D represent the current densities measured under AM 1.5G illumination and in the dark, respectively, while V_{eff} is defined by $V_{eff} = V_0 - V_{bias}$, where V_0 is the voltage when J_{ph} is zero and V_{bias} is the applied bias. Normally, when charges are fully dissociated and sweep out under a high internal electric field, J_{ph} will reach a saturation value (J_{sat}) at the high bias region. Moreover, the $J_{ph,max}/J_{ph,sat}$ ratio can represent the product of charge collection probability under a maximum power output condition, whereas the $J_{ph,sc}/J_{ph,sat}$ ratio can stand for the product of exciton dissociation probability under the short-circuit condition. Hence, the charge dissociation and collection probability can be evaluated from the J_{ph}/J_{sat} ratio under an external bias between the short-circuit condition and the maximum power output condition. As shown, the DBC and DBC@AuNPs devices exhibit a higher probability of 0.49 and 0.57 at $V_{eff} = 0.1$ V than the value (0.46) of the reference ZnO device. This result unveils that both DBC and DBC@AuNPs interlayers indeed improve the charge collection efficiency of the device. Further, the highest value observed in the DBC@AuNPs device suggests its most optimized charge dissociation and collection probability, which might benefit from the plasmon-electrical effects.[16, 17]

We next measure the device's response as a function of light intensity in the range of 20 to 100 mW/cm^2 and **Figure 2d** displays the relationship between V_{oc} and light intensity in log scale. A slope between 1.13-1.30 k_BT/q (where k_B is the Boltzmann constant, T is absolute temperature, and q is elementary charge) was recorded for our fabricated devices, suggesting that a bimolecular recombination process is dominant during device operation.[22] The lower slope observed in the DBC@AuNPs device indicates its less tendency toward trap-assisted charge recombination.[22] In order to understand the defect density in these devices, we analyzed the trap density (N_{trap}) of the ZnO and DBC@AuNPs devices by measuring their I-V response in the SCLC regime according to the following equation: $V_{TFL} = eN_{trap}L^2/(2\varepsilon\varepsilon_0)$, where V_{TFL} is the trap-filled limited voltage, e is the elementary charge, L is the thickness of active layer, ε is the relative dielectric constant of the BHJ layer, and ε_0 is the vacuum permittivity. As depicted in **Figure 2e**, the evaluated V_{TFL} of the DBC@AuNPs device is 0.46 V associated with a N_{trap} of 1.26 x 10^{16} cm^{-3}. Whereas, the V_{TFL} of the ZnO device is increased to 0.62 V associated with a higher N_{trap} of 1.70 x 10^{16} cm^{-3}. This result clearly highlights the advantageous roles of the DBC@AuNPs interlayer for decreasing trap density.

Presented in **Figure 2f** are the external quantum efficiency (EQE) spectra of our fabricated devices. All devices displayed high photo-response across 500-800 nm with a similar profile. Note that the DBC@AuNPs device exhibited a slightly higher photo-response at ~400 nm, which might contribute from Au NPs' absorption through the optical plasmonic effects.[16, 17] We also examined the general applicability of both DBC and DBC@AuNPs interlayers in another NFA BHJ system, PTB7-Th:ITIC BHJ blend. The relevant J-V curves, J_{ph}-V_{eff} characteristics, V_{oc} with light intensity curves, normalized EQE, and photovoltaic performance were presented in **Figure S7** and **Table S3**, and the detailed discussion was described in Supplementary Notes 3. In brief, the results confirm that both DBC and DBC@AuNPs interlayers effectively suppress the interface charge recombination at ZnO/BHJ interface and improve the charge collection efficiency through optimizing the interfacial electronic properties at this corresponding interface.

2.3. Investigation of device's thermal stability

It has been known that the environment conditions, such as thermal, moisture, and light, will impact the operational lifetime of OPVs in different ways.[23] Recent studies have also unveiled that the NFA BHJ system could possess a better thermal stability than the fullerene-based BHJ system. However, there is a dearth of comprehensive characterization and understanding of the impact of thermal stress on the structural evolution in OPVs. Generally, the specific parameter employed to evaluate the stability is the time when device's performance drops to 80% of the initial value (denoted as T_{80} lifetime). We first examine the ambient- and photo-stability of our fabricated devices by storing them in an atmosphere condition of relative humidity (RH) of 50% at 25 ^{o}C and under continuous 1-sun illumination in a home-made container filled with N_2. As revealed, all the devices showed decent ambient stability and comparable T_{80} lifetime (**Figure S8a**) and similar tendency of photo-degradation (**Figure S8b**), manifesting that the moisture and light soaking are not the main key factors to engender difference in our device's operational lifetime.

We next examine the thermal stability of our fabricated devices by aging them at 65 ^{o}C in a glove box (in a nitrogen atmosphere) to exclude the humidity effect. As illustrated in **Figure 3a**, the DBC@AuNPs device owns a much better robustness against high-temperature aging than the other two devices. It exhibits an impressive T_{80} lifetime of 1,100 hours, greatly surpassing the values (408 hours and 260 hours) of the DBC device and the control ZnO device. When taking a closer look at the evolution of photovoltaic parameters of the ZnO device (**Figure 3b**), the drop in *FF* seems to play the major role in performance degradation after aging. According to the previous results, the morphological change of BHJ layer might be the main reason because the thermal-induced micro-phase separation will deteriorate the charge transport and dissociation efficiency.[24] Notably, we also measured the ambient and thermal stability of the devices based on the PTB7-Th:ITIC blend system. As presented in **Figure S9**, the DBC@AuNPs device still showed the highest ambient and thermal stability among the studied devices. However, as compared to the PM6:Y6 system, the PTB7-Th:ITIC system affords an inferior long-term thermal stability, as limited by its poorer intrinsic thermal stability.

To clarify this issue, we first probe the morphological change of the ZnO, ZnO/DBC, and ZnO/DBC@AuNPs ETLs after thermal aging because their morphological change will directly engender the morphological change of atop BHJ layer. **Figure 3c** presents the atomic force microscopy (AFM) images of these ETLs before and after thermal aging. As shown, after aging at 65^{o}C for 150 hours, the morphology of the ZnO/DBC and ZnO/DBC@AuNPs ETLs remains uniform and the surface roughness does not largely change. Whereas, a serious deformation was observed in the aged ZnO ETL, for which the surface roughness was increased from 1.40 nm to 2.27 nm after thermal aging. This result suggests that the morphology at the ZnO/BHJ interface plays a critical role on the discrepant thermal stability as observed earlier. Notably, the superior thermal stability of the DBC@AuNPs device than the DBC device could benefit from the strengthened interactions between the DBC molecules and Au NPs, which endows the DCB@AuNPs with better thermal robustness.

After elucidating the impact of the DBC-based interlayers on the thermal stability of ZnO ETL, we next examine their influence on the morphology of atop BHJ layer. **Figure S10** presented the topographical AFM images of the fresh and thermally-aged (annealed at 65^{o}C for 150 hrs) PM6:Y6 BHJ films grown on the ZnO, ZnO/DBC, and ZnO/DBC@AuNPs ETLs. For all the cases, finely interpenetrating networks formed by PM6 and Y6 were clearly observed before thermal aging. After thermal aging, their morphologies only displayed slight change in surface texture and roughness. Meanwhile, we have also measured the surface energy of the BHJ films before and after thermal aging. As shown in **Table S2**, the surface energy of the studied BHJ films showed negligible changes after thermal aging. These results suggest that no interfacial reaction at the ETL/BHJ interface occurs and the change in device's thermal stability should lie in their respective thermal stability. Nevertheless, it is interesting to note that the surface energy of the BHJ film grown on the ZnO/DBC@AuNPs ETL showed a rare change ($\Delta \gamma$ = 0.16 mN/m) after thermal aging while the film grown on the ZnO ETL delivered the largest change ($\Delta\ \gamma$ = 0.72 mN/m). This result reveals that the DBC-based interlayers are beneficial for stabilizing the BHJ morphology under thermal aging.

To probe more details, we characterized the morphological changes of these BHJ films before and after aging using grazing incidence wide-angle X-ray scattering (GIWAXS). The two-dimensional (2D) GIWAXS patterns of the fresh and aged BHJ films are presented in **Figure 4a**, and their extracted 1D profiles are portrayed in **Figure 4b-4c**. The relevant parameters extracted from GIWAXS measurement are summarized in **Figure 4d** and **Table S4**. As can be observed, the crystallinity of the BHJ films grown on the ZnO/DBC and ZnO/DCB@AuNPs ETLs is enhanced as compared to the BHJ film grown on the pristine ZnO ETL. This improvement is mainly imposed by the use of DBC layer, which changes of surface energy of ZnO to provide a more compatible surface energy with the photoactive components as discussed earlier. Note that the improved crystallinity of the BHJ films might be also one important factor contributing to the enhanced performance of both devices as observed.

Besides, as the results shown in **Figure 4**, the molecular packing pattern of the BHJ film grown on the ZnO/DBC@AuNPs ETL exhibited negligible change in the in-plane and out-of-plane directions after thermal aging; meanwhile, the associated π-π stacking and crystallinity size remain similar after aging. This result clearly reveals that using DBC@AuNPs interlayer is beneficial to stabilize the interfacial morphology at the ZnO/BHJ interface and the BHJ morphology of the photoactive layer.[25] On the contrary, the molecular packing pattern of the BHJ film grown on the ZnO ETL displayed conspicuous changes in the in-plane and out-of-plane directions after aging. As discussed earlier, ZnO ETL itself already exhibited morphological changes after thermal aging. These results thus clearly prove that the inferior thermal stability of the control ZnO device originates from its instable interfacial morphology at the ZnO/BHJ interface and highlights that the interfacial morphology at the ZnO/BHJ interface plays the most important role in governing the resultant thermal stability of the device.

Note that, for the BHJ film grown on a ZnO ETL, a (010)’ diffraction peak in the range of

1.10-1.50 Å^{-1} is observed before thermal aging, which arises from the randomly oriented □-□ stacking of Y6.[26] That is, Y6 tends to keep disordered rather than be aligned with the orientation of PM6 in the blend, resulting in a metastable state of the BHJ morphology.[27] For the BHJ films grown on the ZnO/DBC and ZnO/DBC@AuNPs ETLs, this peak is absent, suggesting the improved miscibility between Y6 and PM6. Such better modulated BHJ morphology partially contributes to the enhanced PCE as shown earlier. It is worthwhile noting that the π-π stacking distance and crystallinity size of the BHJ film grown on the pristine ZnO ETL showed a large change after thermal aging, which can be attributed to its metastable state of the BHJ morphology.[27] Encouragingly, such deficiency can be completely addressed by using the DBC@AuNPs interlayer. It is because it improves the interfacial compatibility at the ZnO/BHJ interface to endows a more ideal BHJ morphology with enhanced thermal stability as discussed. The above result demonstrates that the DBC-based interlayers, especially for the DBC@AuNPs one, not only improves the interfacial thermal stability at the BHJ/ZnO interface but also endows a more ideal BHJ morphology with an enhanced thermal robustness.

At present, the most popular method to predict the lifespan of the material is using Arrhenius relationship.[28] It often requires the extrapolation of accelerated aging data of failure time or degradation rates determined at elevated temperatures to the lifetime prediction. In principle, Arrhenius extrapolations assume that a chemical degradation process is controlled by a degradation rate k_d, which is proportional to exp($-E_a/k_B T$), where E_a is the activation energy of a failure condition, k_B is the Boltzmann constant, and T is the temperature in Kelvin. Since the lifetime to reach a certain degree of degradation ($T_{\%,T}$) at temperature T is theoretically proportional to the reciprocal of degradation rate, Arrhenius relationship thus can be rearranged to the following form: $T_{\%,T} = C \exp\left(\frac{E_a}{K_B T}\right)$. Based on this equation, we measured the lifetime of the DBC@AuNPs device under various aging temperatures (65, 75, and 85^{o}C) in the glove box (an inert condition) as shown in **Figure 3d**. As can be seen, the lifetime of the

DBC@AuNPs device at room temperature (298 K) is estimated to be 15,700 hours, approximately 1.79 years, as illustrated in **Figure 3e**. This result intriguingly unveils that using DBC@AuNPs interlayer can largely improve device's long-term thermal stability to a practical level.

3. Conclusion

We develop an amphiphilic DBC through a facile coupling method and examine its interlayer function in inverted NFA BHJ OPVs. Besides showing distinct self-assembly behavior, we reveal that DBC possesses high compatibility with plasmonic Au NPs due to the constituent malonamide and ethylene oxide units. When using as the surface modifier of ZnO ETL, the hybrid DBC@AuNPs interlayer is shown to improve device's PCE from 14.0% to 15.4%. The enhancement introduced by this interlayer is attributed to the better energy level alignment and improved interfacial compatibility at the ZnO/BHJ interface, which reduces charge recombination in the device. More encouragingly, we demonstrate that the DBC@AuNPs interlayer not only improves the interfacial thermal stability at the ZnO/BHJ interface but also endows a more ideal BHJ morphology with an enhanced thermal robustness. The DBC@AuNPs-based device can reserve 77% of initial PCE after thermal aging at 65^{o}C for 3,000 hours, outperforming the control device. Besides, it exhibits an extended T_{80} lifetime of > 1,100 hours when stored at a constant thermal condition at 65^{o}C. Finally, we show that the T_{80} lifetime of the device at room temperature (298 K) can be over 1.79 years when stored in an inert condition. The results shown in this work might stimulate further research and bring real impact for the future development of OPVs.

4. Experimental Section

Materials. 1-octadecanol was purchased from Alfa Aesar without further purification. Isobutyryl chloride (IBUC), methylene di-p-phenyl diisocyanate (MDI), diethylenetriamine

(DETA), and methanol (MeOH) were purchased from Aldrich. Triethylamine (TEA), xylene, cyclohexane, tetrahydrofuran (THF), ethyl acetate (EA), and *N*,*N*-dimethylformamide (DMF) were purchased from Echo. Magnesium sulfate was purchased from Fisher Scientific. The poly(oxyalkylene)amines Jeffamine®ED2003 was purchased from Huntsman. The dendrons of G2.5 was prepared by grafting stearyl alcohol onto the building block 4-isocyanato-4-(3,3-dimethyl-2,4-dioxo-acetidino)diphenylmethane (IDD) as described in previous reports.[29] The detailed synthesis of DBC was described in Supplementary Note 1. Polymer donors, PTB7-Th and PM6, and NFAs, ITIC and Y6, were purchased from 1-Material (Canada) and used without further purification.

Characterization. ^{1}H-NMR spectra of $CDCl_3$ and DMSO-d_6 solutions were recorded using a Bruker DPX400 MHz FT-NMR spectrometer. IR spectra were recorded using a Jasco 4100 FT-IR spectrometer. Thermogravimetric analysis (TGA) was performed by using a TA Instruments Q50 thermogravimetric analyzer operated at a heating rate of 10°C/min from 100 to 800°C under N_2. The thermal decomposition temperature (T_d) was taken to be the temperature corresponding to 5% weight loss of the sample. The glass transition temperatures (T_g) and phase transition temperatures (T_{ph}) were determined using a TA Instrument DSC Q20 at a heating rate of 10°C/min from 0 to 150°C. Fast atom bombardment mass spectrometry (FABMS) analysis was performed on a JEOL JMS SX/SX 102A mass spectrometer equipped with the standard FAB source, of which the upper limit for measuring molecular weight was 2,000. GPC was conducted by using a Waters apparatus equipped with Waters Styragel columns and a refractive index detector (polystyrene calibration; mobile phase: THF). TEM was performed on a JOEL JEM-1230 with Gatan Dual Vision CCD Camera and operated at 120 kV, and the solution was dipped on a 200 mesh carbon-coated Cu grid for the analyses. Subsequently, specimens were stained by exposing to the vapor of ruthenium tetroxide (RuO_4). The DLS was measured the particle size of DBC. The contact angle (CA) was measured for the surface energy analyses. The AFM images were obtained using a MultiMode AFM system with a Nanoscope 3D controller (Digital Instruments) in a tapping mode. The spring constant of the silicon cantilevers (Nanosensor PPP-SEIHR) was 15 N m^{-1} and the resonant frequency was 130 kHz. UPS was measured by using electron spectroscopy for chemical analysis ULVAC-PHI PHI 5000 Versaprobe II with a He (I) (21.22 eV) light source. A pass energy of 20 eV was used and the take-off angle of the photoelectron with setting at 90^{o}. The *J-V* characteristics of the devices measured under AM 1.5 G illumination (100 mW cm^{-2}) by a xenon-lamp-based solar simulator (AM 1.5G, Enli Tech), and the light intensity of the solar simulator was calibrated by a mono- crystalline silicon solar cell (SRC2020, Enli Tech), which were recorded with a computer-controlled Keithley 2400 source measurement unit (SMU). The illumination intensity was calibrated using a Si photo-diode detector with a KG-5 filter. The EQE was recorded using a monochromatic light from a xenon lamp during the illumination (QE-R, Enlitech Co., Ltd.) and using a standard single crystal Si photovoltaic cell from 300 to 800 nm to calibrate the light intensity of each wavelength. GIWAXS data were conducted on the beamline 8-IDE with a wavelength of 1.6869 Å in the Advanced Photon Source (APS), Argonne National Laboratory (ANL), USA. Typical GIWAXS patterns were taken at an incidence angle of 0.14°.

Synthesis and characterization of DBC. A solution of G2.5 (2.30 g, 0.63 mmol) and ED2003 (0.60 g, 0.30 mmol) in dry THF (15 mL) was stirred at 60 °C under a N_2 atmosphere for 4 hours. After solvent evaporation, the product was purified through column chromatography (SiO_2; EtOAc/hexanes) as a light yellowish viscous liquid (1.51 g, 54%). FT-IR (KBr): 3312 cm^{-1} (NH), 1660 cm^{-1} [C=O(NH)]. ^{1}H-NMR (400 MHz, DMSO-d_6): δ (ppm) = 0.87 (24H, CH_3), 3.79 (28H, Ar-CH_2-Ar), 4.04 (16H, NHCOO-CH2), 7.00-7.52 (112H, Ar-H). GPC (THF): M_n = 9600, M_w = 10330, PDI = 1.08.

Preparation of amphiphilic DBC incorporating Au NPs. The solution of Au NPs with 27 nm was prepared and characterized according to a previous work.[30] Afterwards, the solution of Au NPs is mixed with *DBC* (1/1, v/v) to prepare the precursor solution of DBC@AuNPs.

Device fabrication and characterization. Inverted OPV was fabricated with a device configuration of ITO glass/ZnO/DBCs/BHJ/MoO_3/Ag. The ITO glass substrates were sequentially washed by detergent, deionized water, acetone, and isopropyl alcohol for 15 mins for each solvent. The substrates were then dried by N_2 flow and followed by 10 min plasma treatment. 0.1 g zinc acetate was dissolved in 1 mL of 2-methoxyethanol with 28 μL of ethanolamine to prepare the ZnO precursor. The ZnO layer was spin-coated onto the ITO substrates and annealed at 200^{o}C for 30 min in air. The precursor solutions of DBC were prepared in 2-methoxyethanol with a concentration of 0.1 g mL^{-1}, and the precursor solutions of DBC@AuNPs was prepared by adding Au NPs into DBC (1/1, v/v). The studied amphiphilic DBC-based interlayers were spin-coated onto the ZnO layer and annealed at 130^{o}C for 15 min in air. The precursor solution of PTB7-Th:ITIC blend (1:1 weight ratio) was prepared in CB and the precursor solution of PM6:Y6 blend (1:1.2 weight ratio) was prepared in chloroform (CF) with 1-chloronaphthalene (CN) additive (CF/CN = 99.5/0.5, v/v). All these precursor solutions were vigorously stirred at 60°C for 8 hours in a N_2 glovebox. The NFA-based BHJ layer was spin-coated onto the studied ETL and the thickness was 80-90 nm. For the PM6-based BHJ system, the films were annealed at 110°C for 10 min in a N_2 glovebox. Finally, 8-nm MoO_3 and 100-nm Ag was sequentially thermally deposited under high vacuum (<10^{-6} Torr) to complete the top electrode. The device's active area is 7 mm^2.

Supporting Information

Supporting Information is available from the Wiley Online Library or from the author.

Acknowledgements

C.-C. C. gratefully thanks financial support from the Ministry of Education (109L9006) and the Ministry of Science and Technology in Taiwan (MOST 109-2634-F-002-042 & 108-2221-E-002-026-MY3 & 108-2638-E-002-003-MY2). L. W. gratefully thanks financial support by the

Ministry of Science and Technology (MOST 108-2113-M-002-015-MY3), Academia Sinica (AS-SS-109-05), and the Center of Atomic Initiative for New Materials, National Taiwan University (NTU). L.-Y. S. gratefully thanks financial support from the Ministry of Education (108L4000). H.-H. H. thanks the financial support from 2019 New Partnership Program (108-2911-I-002-561). We also thank Prof. Shih-Huang Tung and Prof. Ru-Jong Jeng for the assistance with synthesis and characterization of materials from the Institute of Polymer Science and Engineering, NTU. This research used resources of the Advanced Photon Source, a U.S. Department of Energy (DOE) Office of Science User Facility operated for the DOE Office of Science by Argonne National Laboratory under Contract No. DE-AC02-06CH11357. This research used synchrotron resources from the Advanced Photon Source (APS) of Argonne National Laboratory. This work was performed, in part, at the Center for Integrated Nanotechnologies, an Office of Science User Facility operated for the U.S. Department of Energy (DOE) Office of Science by Los Alamos National Laboratory (Contract 89233218CNA000001).

Received: ((will be filled in by the editorial staff))
Revised: ((will be filled in by the editorial staff))
Published online: ((will be filled in by the editorial staff))

References

[1] a) Y. Cui, H. Yao, L. Hong, T. Zhang, Y. Xu, K. Xian, B. Gao, J. Qin, J. Zhang, Z. Wei, *Advanced Materials* **2019**, 31, 1808356; b) L. Hong, H. Yao, Z. Wu, Y. Cui, T. Zhang, Y. Xu, R. Yu, Q. Liao, B. Gao, K. Xian, *Advanced Materials* **2019**, 31, 1903441; c) L. Zhan, S. Li, T.-K. Lau, Y. Cui, X. Lu, M. Shi, C.-Z. Li, H. Li, J. Hou, H. Chen, *Energy & Environmental Science* **2020**, 13, 635; d) S. Li, L. Zhan, Y. Jin, G. Zhou, T.-K. Lau, R. Qin, M. Shi, C.-Z. Li, H. Zhu, X. Lu, F. Zhang, H. Chen, *Advanced Materials* **2020**, 32, 2001160; e) Y. Cui, H. Yao, L. Hong, T. Zhang, Y. Tang, B. Lin, K. Xian, B. Gao, C. An, P. Bi, W. Ma, J. Hou, *National Science Review* **2019**, 7, 1239.

[2] a) P. Cheng, G. Li, X. Zhan, Y. Yang, *Nature Photonics* **2018**, 12, 131; b) Z. a. Li, C.-C. Chueh, A. K. Y. Jen, *Progress in Polymer Science* **2019**, 99, 101175.

[3] a) Z. He, C. Zhong, S. Su, M. Xu, H. Wu, Y. Cao, *Nature photonics* **2012**, 6, 591; b) C.-C. Chueh, C.-Z. Li, A. K.-Y. Jen, *Energy & Environmental Science* **2015**, 8, 1160;

c) Y. Liu, V. V. Duzhko, Z. A. Page, T. Emrick, T. P. Russell, *Accounts of chemical research* **2016**, 49, 2478.

[4] a) Z. Hu, Z. Zhong, Y. Chen, C. Sun, F. Huang, J. Peng, J. Wang, Y. Cao, *Advanced Functional Materials* **2016**, 26, 129; b) C. Sun, Z. Wu, Z. Hu, J. Xiao, W. Zhao, H.-W. Li, Q.-Y. Li, S.-W. Tsang, Y.-X. Xu, K. Zhang, *Energy & Environmental Science* **2017**, 10, 1784; c) C. Wang, Y. Luo, J. Zheng, L. Liu, Z. Xie, F. Huang, B. Yang, Y. Ma, *ACS applied materials & interfaces* **2018**, 10, 10270.

[5] P. Li, G. Wang, L. Cai, B. Ding, D. Zhou, Y. Hu, Y. Zhang, J. Xiang, K. Wan, L. Chen, *Physical Chemistry Chemical Physics* **2014**, 16, 23792.

[6] a) J. B. Park, M. Isik, H. J. Park, I. H. Jung, D. Mecerreyes, D.-H. Hwang, *ACS applied materials & interfaces* **2018**, 10, 4887; b) V. Mitchell, D. Jones, *Polymer Chemistry* **2018**, 9, 795; c) K.-T. Huang, C.-C. Shih, B.-H. Jiang, R.-J. Jeng, C.-P. Chen, W.-C. Chen, *Journal of Materials Chemistry C* **2019**, 7, 12572.

[7] a) M. Lv, S. Li, J. J. Jasieniak, J. Hou, J. Zhu, Z. a. Tan, S. E. Watkins, Y. Li, X. Chen, *Advanced Materials* **2013**, 25, 6889; b) T.-Y. Juang, Y.-C. Hsu, B.-H. Jiang, C.-P. Chen, *Macromolecules* **2016**, 49, 7837; c) M. Rafiq, Z. Chen, H. Tang, Z. Hu, X. Zhang, Y. Xing, Y. Li, F. Huang, *ACS Applied Polymer Materials* **2019**.

[8] a) N. Li, I. McCulloch, C. J. Brabec, *Energy & Environmental Science* **2018**, 11, 1355; b) C. Zhang, T. Heumueller, S. Leon, W. Gruber, K. Burlafinger, X. Tang, J. D. Perea, I. Wabra, A. Hirsch, T. Unruh, N. Li, C. J. Brabec, *Energy & Environmental Science* **2019**, 12, 1078; c) Y. He, T. Heumüller, W. Lai, G. Feng, A. Classen, X. Du, C. Liu, W. Li, N. Li, C. J. Brabec, *Advanced Energy Materials* **2019**, 9, 1900409; d) K.-E. Hung, C.-E. Tsai, S.-L. Chang, Y.-Y. Lai, U. S. Jeng, F.-Y. Cao, C.-S. Hsu, C.-J. Su, Y.-J. Cheng, *ACS Applied Materials & Interfaces* **2017**, 9, 43861.

[9] a) R. S. Gurney, D. G. Lidzey, T. Wang, *Reports on Progress in Physics* **2019**, 82, 036601; b) L. Ye, B. A. Collins, X. Jiao, J. Zhao, H. Yan, H. Ade, *Advanced Energy Materials* **2018**, 8, 1703058; c) H. Lee, C. Park, D. H. Sin, J. H. Park, K. Cho, *Advanced Materials* **2018**, 30, 1800453.

[10] a) E. M. Speller, A. J. Clarke, J. Luke, H. K. H. Lee, J. R. Durrant, N. Li, T. Wang, H. C. Wong, J.-S. Kim, W. C. Tsoi, Z. Li, *Journal of Materials Chemistry A* **2019**, 7, 23361; b) J. Min, C. Cui, T. Heumueller, S. Fladischer, X. Cheng, E. Spiecker, Y. Li, C. J. Brabec, *Advanced Energy Materials* **2016**, 6, 1600515.

[11] a) T. Kim, J. Choi, H. J. Kim, W. Lee, B. J. Kim, *Macromolecules* **2017**, 50, 6861; b) W. Wang, B. Chen, X. Jiao, J. Guo, R. Sun, J. Guo, J. Min, *Organic Electronics* **2019**, 70, 78.

[12] a) K. Sivula, C. K. Luscombe, B. C. Thompson, J. M. J. Fréchet, *Journal of the American Chemical Society* **2006**, 128, 13988; b) S. Bertho, B. Campo, F. Piersimoni, D. Spoltore, J. D'Haen, L. Lutsen, W. Maes, D. Vanderzande, J. Manca, *Solar Energy Materials and Solar Cells* **2013**, 110, 69.

[13] P. Cheng, C. Yan, T.-K. Lau, J. Mai, X. Lu, X. Zhan, *Advanced Materials* **2016**, 28, 5822.

[14] a) G. Griffini, J. D. Douglas, C. Piliego, T. W. Holcombe, S. Turri, J. M. J. Fréchet, J. L. Mynar, *Advanced Materials* **2011**, 23, 1660; b) C.-P. Chen, C.-Y. Huang, S.-C. Chuang, *Advanced Functional Materials* **2015**, 25, 207; c) W. Feng, Z. Lin, J. Cui, W. Lv, W. Wang, Q. Ling, *Solar Energy Materials and Solar Cells* **2019**, 200, 109982.

[15] a) J. N. Israelachvili, D. J. Mitchell, B. W. Ninham, *Journal of the Chemical Society, Faraday Transactions 2: Molecular and Chemical Physics* **1976**, 72, 1525; b) J. Israelachvili, S. Marčelja, R. G. Horn, *Quarterly reviews of biophysics* **1980**, 13, 121; c) J. N. Israelachvili, *Intermolecular and surface forces*, Academic press, **2011**.

[16] a) E. Stratakis, E. Kymakis, *Materials Today* **2013**, 16, 133; b) W. C. H. Choy, X. Ren, *IEEE J. Sel. Top. Quantum Electron* **2016**, 22, 1. c) Z. Y. Bao, S. Liu, Y. Hou, A. Shang, F. Yan, Y. Wu, D. Lei, J. Dai, *Journal of Materials Chemistry A* **2019**, 7, 26797.

[17] a) X. Yang, C. C. Chueh, C. Z. Li, H. L. Yip, P. Yin, H. Chen, W. C. Chen, A. K. Y. Jen, *Advanced Energy Materials* **2013**, 3, 666; b) G. Kakavelakis, E. Stratakis, E. Kymakis, *Chemical Communications* **2014**, 50, 5285; c) A. Singh, A. Dey, P. K. Iyer, *Solar Energy* **2018**, 173, 429.

[18] a) J. Yu, Y. Xi, C.-C. Chueh, J.-Q. Xu, H. Zhong, F. Lin, S. B. Jo, L. D. Pozzo, W. Tang, A. K. Y. Jen, *Nano Energy* **2017**, 39, 454; b) P.-C. Lin, Y.-T. Wong, Y.-A. Su, W.-C. Chen, C.-C. Chueh, *ACS Sustainable Chemistry & Engineering* **2018**, 6, 14621.

[19] X. Bulliard, S. G. Ihn, S. Yun, Y. Kim, D. Choi, J. Y. Choi, M. Kim, M. Sim, J. H. Park, W. Choi, *Advanced Functional Materials* **2010**, 20, 4381.

[20] B.-H. Jiang, Y.-J. Peng, C.-P. Chen, *Journal of Materials Chemistry A* **2017**, 5, 10424.

[21] Y.-Y. Hsu, S.-C. Yeh, S.-H. Lin, C.-T. Chen, S.-H. Tung, R.-J. Jeng, *Reactive and Functional Polymers* **2016**, 108, 86.

[22] H. C. Jin, S. A. Salma, D. K. Moon, J. H. Kim, *Journal of Materials Chemistry A* **2020**, 8, 4562.

[23] W. R. Mateker, M. D. McGehee, *Advanced Materials* **2017**, 29, 1603940.

[24] M. Chang, L. Meng, Y. Wang, X. Ke, Y.-Q.-Q. Yi, N. Zheng, W. Zheng, Z. Xie, M. Zhang, Y. Yi, *Chemistry of Materials* **2020**, 32, 2593.

[25] N. Gasparini, M. Salvador, S. Strohm, T. Heumueller, I. Levchuk, A. Wadsworth, J. H. Bannock, J. C. de Mello, H.-J. Egelhaaf, D. Baran, I. McCulloch, C. J. Brabec, *Advanced Energy Materials* **2017**, 7, 1700770.

[26] Y. Qin, M. A. Uddin, Y. Chen, B. Jang, K. Zhao, Z. Zheng, R. Yu, T. J. Shin, H. Y. Woo, J. Hou, *Advanced Materials* **2016**, 28, 9416.

[27] J. Xin, X. Meng, X. Xu, Q. Zhu, H. B. Naveed, W. Ma, *Matter* **2019**, 1, 1316.

[28] a) S. Schuller, P. Schilinsky, J. Hauch, C. Brabec, *Applied Physics A* **2004**, 79, 37; b) H.-H. Huang, Y.-C. Shih, L. Wang, K.-F. Lin, *Energy & Environmental Science* **2019**, 12, 1265.

[29] a) C. P. Chen, S. A. Dai, H. L. Chang, W. C. Su, R. J. Jeng, *Journal of Polymer Science Part A: Polymer Chemistry* **2005**, 43, 682; b) S. A. Dai, T. Y. Juang, C. P. Chen, H. Y. Chang, W. J. Kuo, W. C. Su, R. J. Jeng, *Journal of applied polymer science* **2007**, 103, 3591.

[30] C.-Y. Chiang, T.-Y. Liu, Y.-A. Su, C.-H. Wu, Y.-W. Cheng, H.-W. Cheng, R.-J. Jeng, *Polymers* **2017**, 9, 93.

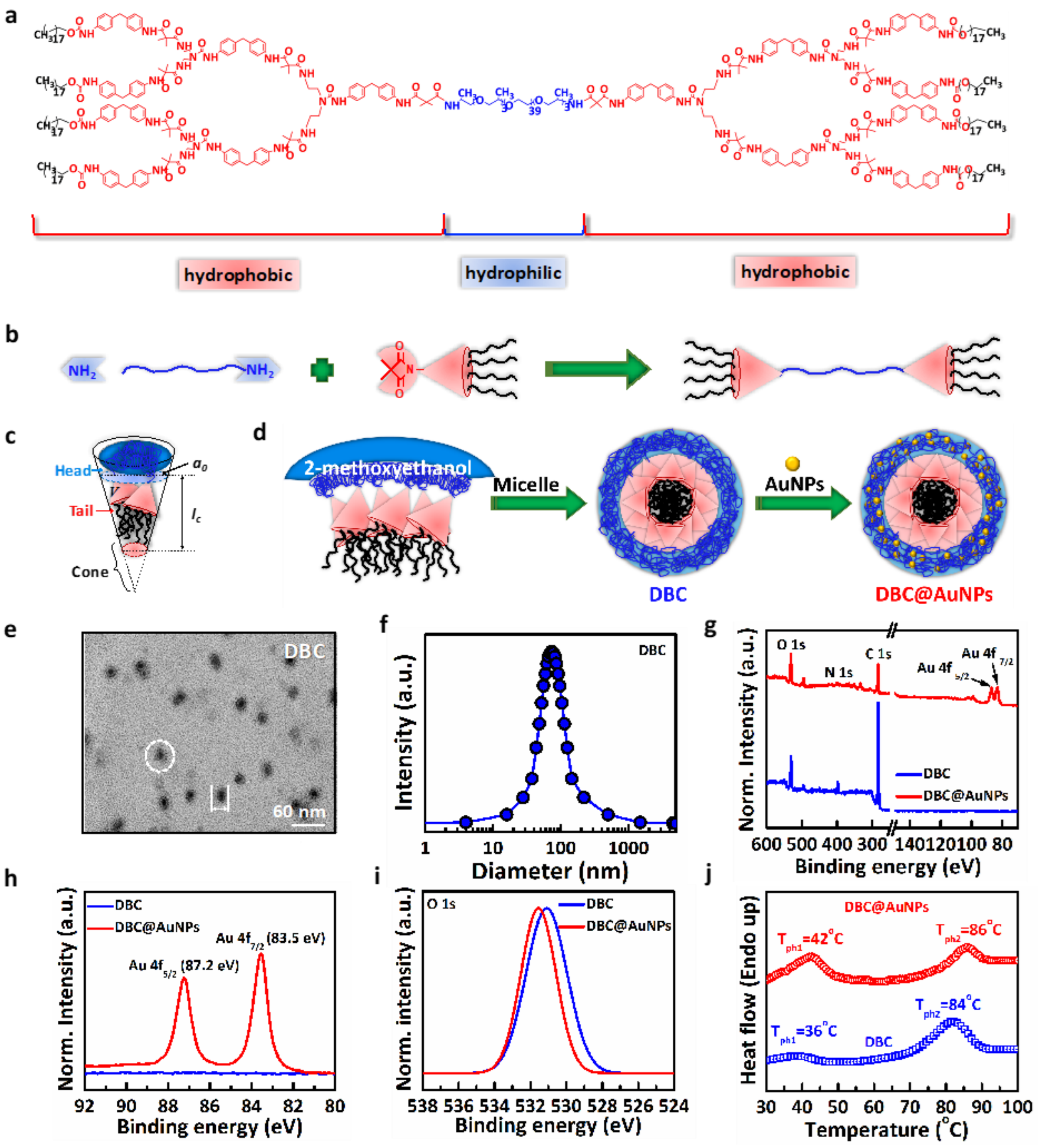

Figure 1. (a) Chemical structure and (b) the schematic reaction route of the studied DBC. Schematic illustration of (c) the conical shape of DBC using the CPP method and (d) the self-assembly micelle of DBC and chelating of Au NPs with the hydrophilic moieties of DBC. (e) TEM image of DBC and (f) their diameter size measured by DLS. (g) Survey scan spectra of the films of DBC and DBC@AuNPs measured by XPS. The corresponding XPS spectra of (h) Au 4f and (i) O 1s for both films. (j) DSC curves of DBC and DBC@AuNPs.

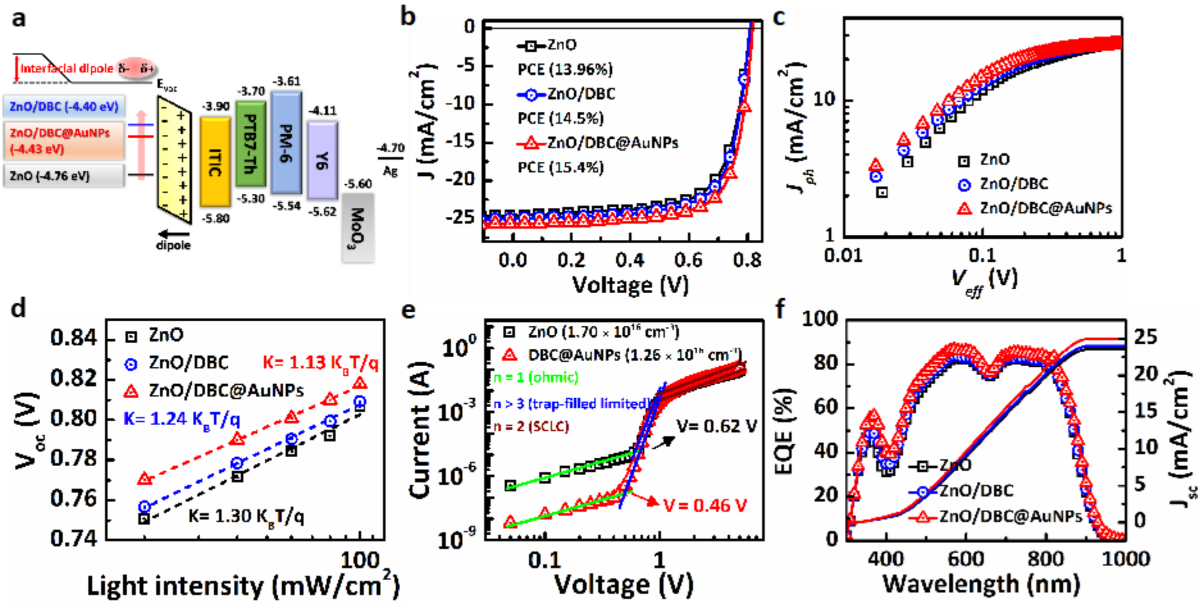

Figure 2. (a) Schematic illustration of the energy-level diagram of our fabricated devices; (b) The *J*-*V* curves, (c) J_{ph}-V_{eff} characteristics, (d) V_{oc} with light intensity curves, (e) current-voltage traces and trapping density, and (f) EQE of our fabricated PM6:Y6 BHJ OPVs using a ZnO ETL and the DBC-modified ZnO ETLs.

Table 1. Photovoltaic parameters of the fabricated PM6:Y6 BHJ OPVs using a ZnO ETL and the DBC-modified ZnO ETLs.

Interlayer	**V_{oc} (V)**	**J_{sc} (mA/cm^2)**	**FF (%)**	**PCE (%)**	**R_{sh} (Ωcm^2)**	**R_s (Ωcm^2)**
None	0.807	24.50 (24.08)[a]	70.6	13.96	532	3.65
	(0.808±0.002)	(24.38±0.22)	(70.19±0.18)	(13.83±0.18)[b]		
DBC	0.809	24.90 (24.52)[a]	71.7	14.50	946	2.49
	(0.810±0.002)	(24.70±0.10)	(70.72±0.17)	(14.13±0.15)[b]		
DBC@ AuNPs	0.818	25.70 (25.50)[a]	73.1	15.40	3248	2.21
	(0.820±0.001)	(25.37±0.24)	(72.74±0.29)	(15.03±0.26)[b]		

[a] Data from EQE measurement; [b] The average PCE shown in the parentheses are based on 15 devices.

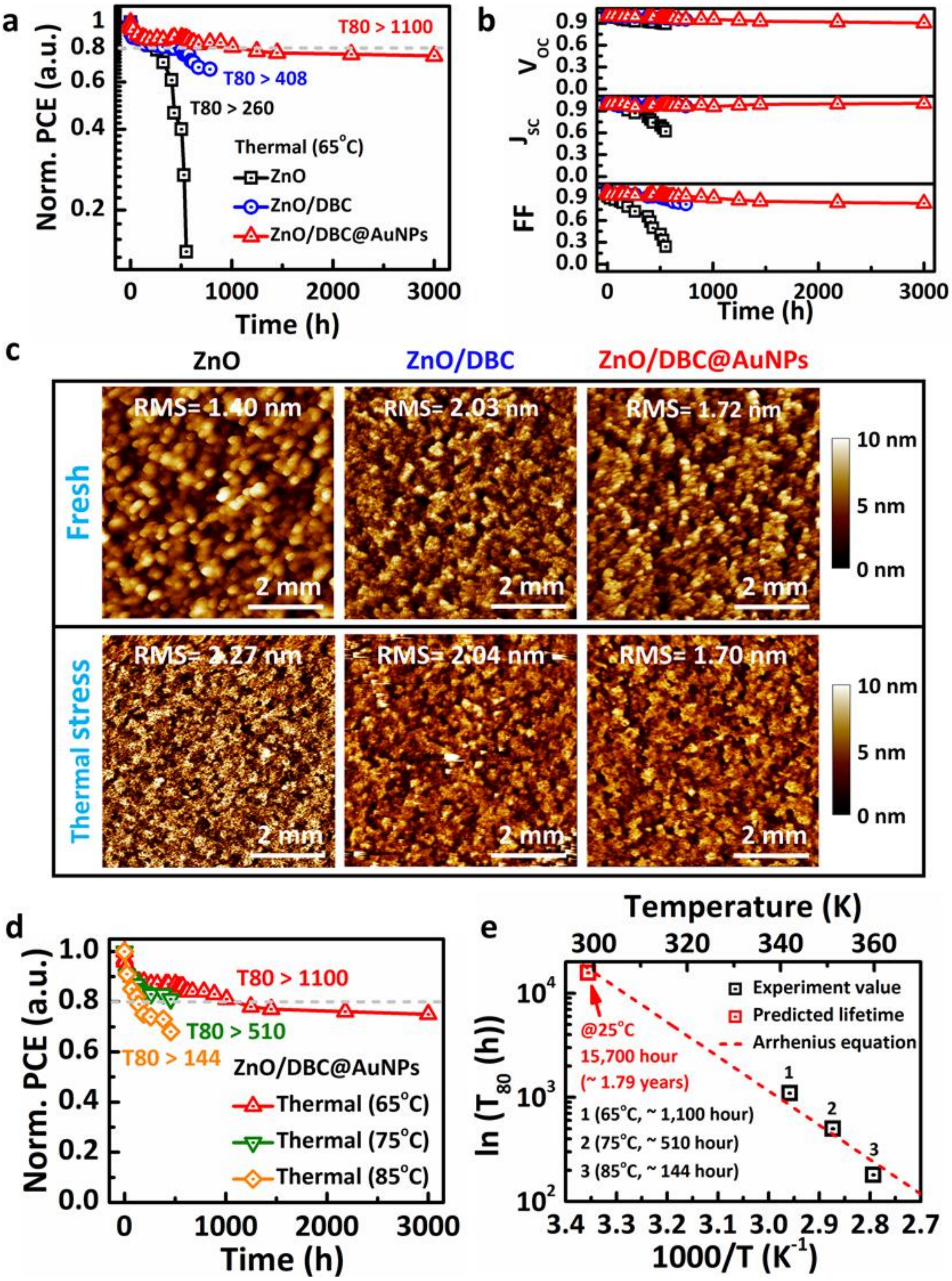

Figure 3. (a) Normalized PCE, (b) V_{oc}, J_{sc}, and *FF* of the studied OPVs as a function of annealing time in the glove box. (c) The topographical AFM images of the fresh ZnO ETL, fresh DBC-modified ZnO ETLs, and these ETLs after thermal aging (annealed at 65°C for 150 hours). (d) Normalized PCE of the DBC@AuNPs device under thermal aging at 65, 75, and 85°C in the glove box. (e) T_{80} of the DBC@AuNPs device versus reciprocal of testing temperature (the dashed line shows the fitting result).

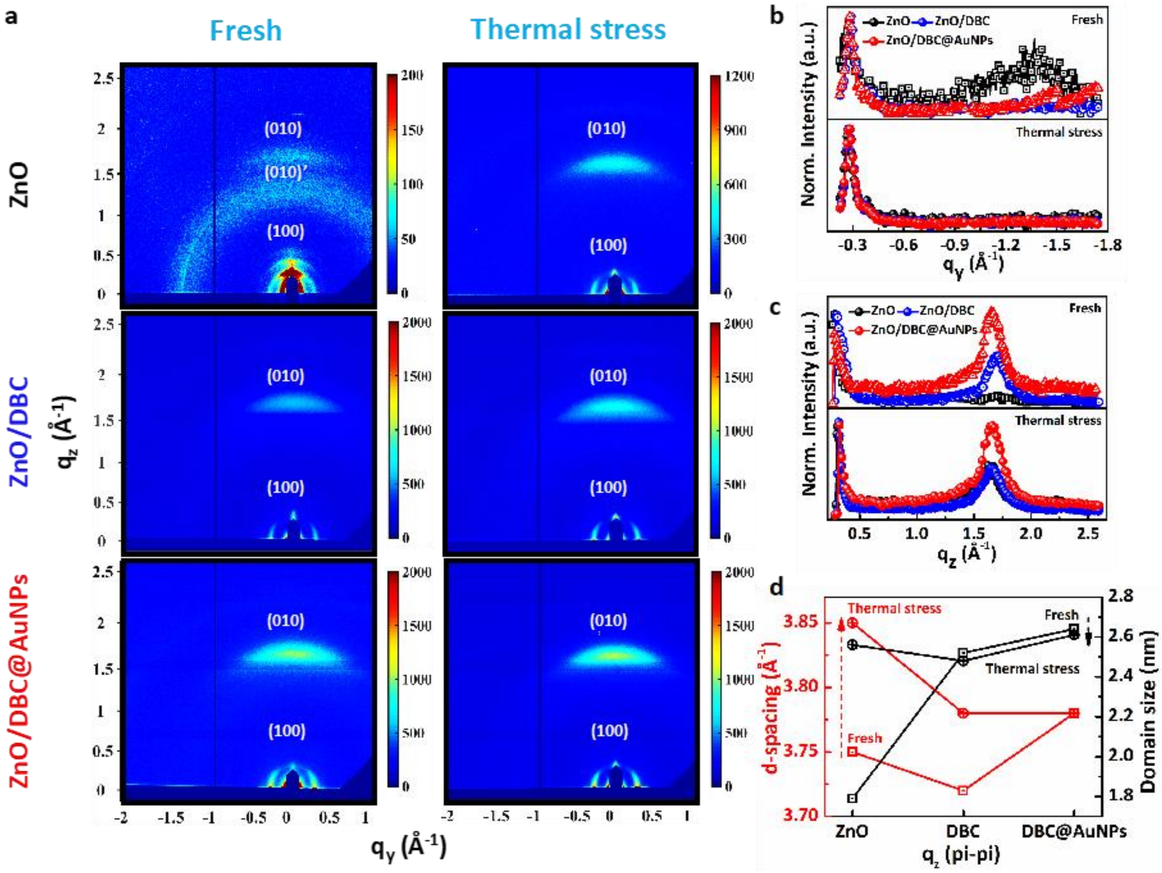

Figure 4. (a) 2D GIWAXS patterns of the PM6:Y6 BHJ film grown on different ETLs before and after thermal stress (annealed at 65ºC for 150 hours). The corresponding 1D linecuts at (b) in-plane direction and (c) out-of-plane direction of the PM6:Y6 BHJ films. (d) The □-□ stacking versus domain size and *d*-spacing in out-of-plane direction.

An amphiphilic dendritic block copolymer (DBC) is developed to serve as an efficient surface modifier of ZnO electron-transporting layer in an organic photovoltaic device. When using an interlayer based on its hybridization with Au NPs (DBC@AuNPs), the power conversion efficiency of the device can be improved from 14.0% to 15.4%. Moreover, the device shows a much enhanced thermal stability, delivering a lifetime of > 1,100 hours when stored at a constant thermal condition at 65°C and a lifetime of over 1.79 years when stored at room temperature in an inert condition.

Keywords: Dendritic block copolymers, self-assembly, metal nanoparticles, interfacial modification, thermal stability

Li-Yun Su,[a,b,c] *Hsin-Hsiang Huang,*[b,d,e] *Yan-Cheng Lin,*[a] *Guan-Lin Chen,*[b] *Wen-Chang Chen,*[a,f] *Wei Chen,*[e,g] *Leeyih Wang,*[b,h,*] *and Chu-Chen Chueh*[a,f,*]

Enhancing Long-Term Thermal Stability of Non-Fullerene Organic Solar Cells Using Self-Assembly Amphiphilic Dendritic Block Copolymer Interlayers